Basin width control of faulting in the Naryn Basin, south-central Kyrgyzstan

Joseph K. Goode,[1] Douglas W. Burbank,[1] and Bodo Bookhagen[2]

Received 11 March 2011; revised 26 August 2011; accepted 2 September 2011; published 10 November 2011.

[1] In Central Asia's Tien Shan, deformation is distributed across the wide orogen, a characteristic of intracontinental mountain building. Active faults are commonly found within intramontane basins that separate its constituent ranges. In order to explore the controls on this intramontane basin deformation, we study the Naryn Basin of south-central Kyrgyzstan. A series of five balanced cross-sections reveals a transition in patterns of faulting from faults confined to basin margins to faults focused within the basin center. The 20-km-wide eastern Naryn Basin displays deformation attributed to low-angle splays of the northern, basin-bounding fault. In the 40-km-wide western Naryn Basin, the pattern of deformation linked to the northern range remains, but is accompanied by steeper faults that dip both south and north without being directly linked to the basin-bounding fault. We compare these cross-sections to synthetic aperture radar interferometry (InSAR) measurements of surface deformation. Profiles of InSAR-derived surface deformation rates across the Naryn Basin reveal that in the west, deformation is distributed across the broad basin interior, whereas in the east, rapid uplift is concentrated at the margin of the narrower basin. From the geodetic and structural data, we infer that in the western Naryn Basin, deformation has migrated away from the northern basin margin and into the interior. Deformation of the eastern basin interior, however, remains linked to the basin-bounding fault. A simple mechanical model demonstrates that basin width may control basin deformation whereby basin-interior faulting in the narrow, eastern Naryn Basin is inhibited by the overburden of adjacent ranges.

Citation: Goode, J. K., D. W. Burbank, and B. Bookhagen (2011), Basin width control of faulting in the Naryn Basin, south-central Kyrgyzstan, *Tectonics*, *30*, TC6009, doi:10.1029/2011TC002910.

1. Introduction

[2] Deformation of the Tien Shan, central Asia's largest mountain range, is driven by the distant collision between India and Asia. The east-west trending ranges of the Central Tien Shan (Figure 1) sit more than 1000 km north of this collision, yet they accommodate approximately 20 mm/y (~50%) of Indo-Asian shortening [*Abdrakhmatov et al.*, 1996; *Molnar and Ghose*, 2000; *Reigber et al.*, 2001; *Zubovich et al.*, 2010]. Even though some of this shortening is absorbed across constructional structures at the margins of the mountain belt [*Bullen et al.*, 2003; *Charreau et al.*, 2008; *Chen et al.*, 2007a; *Daëron et al.*, 2007; *Hubert-Ferrari et al.*, 2007; *Scharer et al.*, 2006], much of the shortening is accommodated within interior of the orogen [*Ghose et al.*, 1998; *Thompson et al.*, 2002; *Zubovich et al.*, 2010]. The growth of multiple individual ranges across the broad (~400 km) orogen attests to the distributed nature of the shortening that over millions of years and has formed multiple intramontane basins separated by fault-bounded ranges [*Burbank et al.*, 1999; *Cobbold et al.*, 1996; *Tapponnier and Molnar*, 1979]. Even though the topography suggests a long-term deformation pattern in which ranges are thrust over intervening basins, today's active faults are commonly found within basin interiors, 10–20 km distant from bedrock-cored ranges [*Avouac et al.*, 1993; *Bullen et al.*, 2003; *Ghose et al.*, 1997; *Korjenkov et al.*, 2007; *Park et al.*, 2003; *Thompson et al.*, 2002]. Geologic measurements of shortening rates averaged over the last 10^4 y [*Thompson et al.*, 2002] are consistent with GPS derived rates across the Kyrgyz Tien Shan. Over this period, the basins themselves are deforming, and faults cutting basin interiors accommodate most of the shortening. Many such basin-interior faults have been linked to steep reverse faults that accommodate uplift of basin-bounding ranges [*Abdrakhmatov et al.*, 2001; *Avouac et al.*, 1993; *Charreau et al.*, 2008; *Thompson et al.*, 2002].

[3] We focus on one basin within the Kyrgyz Tien Shan, the Naryn Basin, to gain insight into how a basin within the rapidly deforming orogen accommodates shortening. The Naryn Basin (Figure 2) extends for 200 km from east to west.

[1]Department of Earth Science, University of California, Santa Barbara, California, USA.
[2]Department of Geography, University of California, Santa Barbara, California, USA.

0278-7407/11/2011TC002910

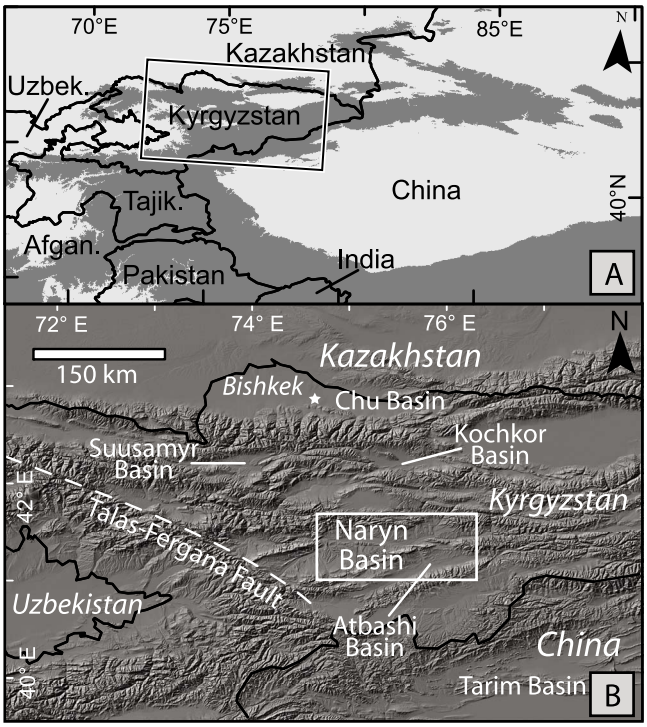

Figure 1. (a) Map of Central Asia highlighting regions with elevation greater than 2000 m. Rectangle marks the region of the Kyrgyz Tien Shan shown in Figure 1b. (b) Shaded relief across the Kyrgyz Tien Shan. Intramontane basins referred to in the text are labeled. The region of the Naryn Basin pictured in Figure 2 is marked with a rectangle.

The western margin of the basin abuts the dextral Talas-Fergana fault [*Burtman et al.*, 1996], which may influence the deformation pattern of the westernmost Naryn Basin, a region also known as the Alabuga Basin. We limit our focus to the eastern 160 km of the basin where contractional folding and dip-slip faulting dominate. This portion of the basin is widest (40 km) in the west and narrows to <15 km in the east. Similar to other basins in the Central Tien Shan, most active faults and folds are observed within the basin interior, rather than along the margins [*Burbank et al.*, 1999; *Thompson et al.*, 2002].

[4] As is also seen in other intramontane basins of the Tien Shan, active structures developed in the Cenozoic fill within the Naryn Basin appear to be young relative to the basin-bounding faults [*Abdrakhmatov et al.*, 2001; *Burbank et al.*, 1999; *Thompson et al.*, 2002]. This contrast implies a migration of deformation away from the range-front fault system to new structures within the basin interior. Both numerical models [*Hilley et al.*, 2005; *Masek and Duncan*, 1998; *Sobel*, 2003] and analog models, e.g., *Cobbold et al.* [1993], of compressional mountain-building regimes indicate that topographic loads may control the migration of deformation into basins.

[5] Before considering the controls on Naryn Basin deformation, we must evaluate whether the migration of deformation into the Naryn Basin represents a relatively superficial change in which the range-front fault system may remain active at depth and transmit that deformation into the basin along lower-angle faults, or whether migration results from a more profound shift in deformation onto newly active faults that cut the bedrock underlying the basin interior.

[6] In order to examine the controls on this younger generation of basin-interior structures, this study incorporates both modern interseismic strain observed with radar interferometry and geologic deformation illustrated through balanced cross-sections. This unusual combination of geodesy, structural mapping and interpretation, and numerical modeling of deformational controls relies on a simplified approach to each of these elements. For example, our balanced cross-sections use numerical approaches that contain only a few models of fold growth. In particular, detachment-style folding and long-wavelength flexure are absent. Given unavoidable uncertainties in cross sections, a rigorous, site-by-site inversion of geodetic signal from InSAR to determine fault geometry or slip distribution is impractical. Instead, we check for consistency between the geodetic signal and our proposed fault geometry. Finally, we use a highly simplified model to describe the effect of basin geometry on fault strength.

[7] We find evidence for both low-angle fault splays that cause basin-interior deformation, but are part of the long-

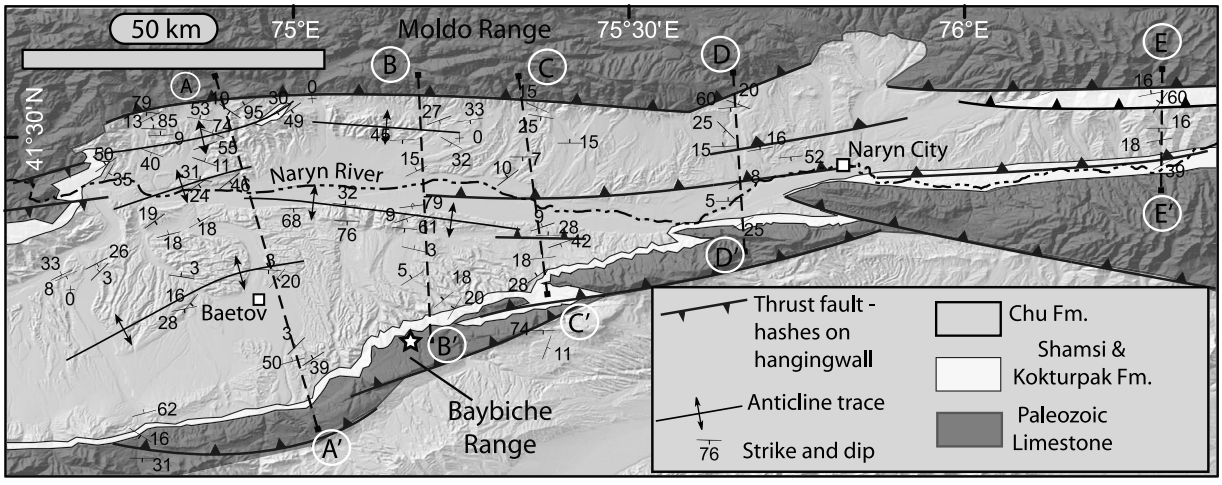

Figure 2. Simplified structural map of the Naryn Basin. Data are based on our own observations as well as those of *Omuraliev* [1988] and *McLean* [1999]. Cross-sections A-A′ through E-E′ are illustrated in Figure 5. The star on the north flank of the Baybiche Range indicates the region shown in Figure 13.

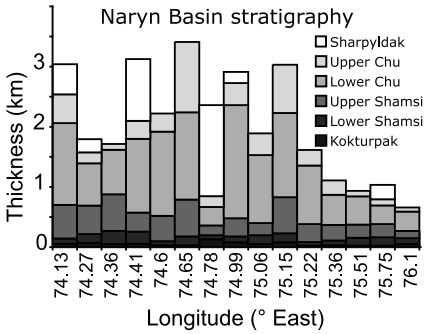

Figure 3. A series of 15 stratigraphic sections modified from *Omuraliev* [1978]. Correlation of Soviet-era stratigraphic terms to formation names currently used in English-language publications is based on a redescription of the section at 75.36°E.

established, range-front fault system, as well as a second suite of structures within the basin interior that are not linked to the range front. Our geometrical loading model indicates that these different structural styles may be a consequence of changes in the width of sediment-filled basins that are bounded by fault-controlled, high bedrock ranges.

2. Geologic and Geomorphic Setting of the Naryn Basin

[8] Several kilometers of Cenozoic strata fill many of the basins in and around the Kyrgyz Tien Shan [*Abdrakhmatov et al.*, 2001; *Charreau et al.*, 2008; *Daëron et al.*, 2007; *Omuraliev*, 1978]. Bedrock exposed in the constituent ranges of the Tien Shan records a history of mountain building that predates the Cenozoic expression of the Tien Shan [*Burtman*, 1975; *Sengör and Natal'in*, 1996; *Windley et al.*, 2007]. The limestone ranges surrounding the Naryn Basin have been interpreted to represent a Paleozoic marine carbonate platform that was amalgamated into the Asian continent during this earlier stage of orogenesis [*Sengör and Natal'in*, 1996]. A long period of tectonic quiescence is represented by a regionally extensive unconformity surface that was beveled across Paleozoic units. This unconformity surface is now exposed on the flanks of many ranges and provides a regional strain marker [*Abdrakhmatov et al.*, 2001; *Burbank et al.*, 1999; *Chediya*, 1986; *Omuraliev and Korzhenkov*, 1995]. Structural contours representing the top of this surface drawn through exposed remnants in uplifted ranges and continued into surrounding basins based on well and geophysical data [*Abdrakhmatov et al.*, 2001; *Cobbold et al.*, 1996] reveal that this surface currently has 14 km of relief across the Kyrgyz Tien Shan and at least 6 km across the Naryn Basin.

[9] A series of 15 measured stratigraphic sections from the Naryn Basin margins compiled from the work of *Omuraliev* [1978] indicates that at least 3.5 km of Cenozoic strata accumulated atop the regional unconformity surface in the Naryn Basin (Figure 3). The remarkably uniform thickness of 30–130 m of the basal Kokturpak formation across a distance of >100 km attests to the exceedingly low initial relief of the underlying unconformity surface. The Kokturpak Formation, a brick-red sandstone and carbonate-cemented breccia and conglomerate, is distinguishable from the overlying Shamsi Formation by its higher silt content and deeper red color. The Shamsi is a reddish sandstone and gravel conglomerate 220–830 m thick. These red basal units also contain gypsum beds greater than 1 m thick that may have acted as detachment surfaces during subsequent deformation. The gray-green sand and siltstones of the overlying Chu formation make up the bulk of the Cenozoic section (>2.5 km; Figure 3). The apparent increase in sediment accommodation space represented by the Shamsi formation has been interpreted to indicate the onset of Cenozoic tectonism in the Kyrgyz Tien Shan, whereas the lacustrine sequences found in the finer-grained Chu formation may imply deposition in relatively restricted intramontane basins [*Abdrakhmatov et al.*, 2001]. Spatially limited and likely asynchronous deposits of coarse, locally derived conglomerate (Sharpyldak Formation) adjacent to the basin margin are commonly interbedded with the predominantly fine-grained Chu in outcrops near both the northern and southern basin margin. The inclusion of locally derived conglomerates in the basin-filling strata indicates that the surrounding ranges were already uplifted and exposed to erosion during at least the later stages of basin-sediment accumulation.

[10] Abandoned fluvial terraces dominate the landscape of the Naryn Basin. These surfaces have been correlated among different drainages based on morphology [*Abdrakhmatov*, 1988; *Omuraliev*, 1978, 1988] and absolute chronology [*Thompson et al.*, 2002]. The terrace surfaces are underlain by gravel and cobble conglomerates that range from 2 to >30 m thickness.

[11] Geophysical and seismological studies across the Kyrgyz Tien Shan place limits on probable fault geometries at depth. A magnetotelluric study from 100 km northwest of the Naryn Basin on the Kochkor Basin margin fault system indicates that low-angle faults near the surface merge at depth with a master fault that dips at 45° ± 15° [*Park et al.*, 2003]. Similarly, aftershocks of the 1992 Sussamyr earthquake centered 140 km northwest of the Naryn basin defined a 50° ± 13° dipping fault plane [*Mellors et al.*, 1997]. The main shock was located near the base of seismicity at 17 km. Together these observations suggest that faults with relatively steep dips (~45°) typically cut the entire brittle crust to depths of about 17 km.

3. Methods

3.1. Interseismic Deformation

[12] Synthetic Aperture Radar Interferometry (InSAR) has gained prominence in recent decades as a tool to observe deformation of the earth surface over short time scales with very high spatial resolution [*Bürgmann et al.*, 2006; *Fielding et al.*, 2004; *Massonnet et al.*, 1993]. This satellite-based remote-sensing technique can provide a snapshot, an interferogram, of surface deformation occurring during time periods ranging from less than a day of coseismic deformation to over a decade of interseismic strain. We use InSAR in the Naryn Basin in order to image interseismic surface deformation over a 5-year period (October 18, 2004–June 13, 2009) (Table 1). (Interferograms are available as auxiliary material.)[1]

[1]Auxiliary materials are available in the HTML. doi:10.1029/2011TC002910.

Table 1. InSAR Scenes

Interferogram	Date SAR Acquisitions (YYYY/MM/DD)	Orbit	Baseline Separation (m)	Time Span (years)
1	2004/05/15	11539	75	2.0
1	2006/05/20	22060	75	2.0
2	2004/06/19	12040	15	3.0
2	2007/06/09	27571	15	3.0
3	2004/07/24	12541	34	4.9
3	2009/06/13	38092	34	4.9
4	2003/10/18	8533	32	1.7
4	2005/07/09	17551	32	1.7
5	2005/09/17	18553	28	3.6
5	2009/05/09	37591	28	3.6
6 (not used)	2004/10/02	13543	34	0.7
6 (not used)	2005/06/04	17050	34	0.7

[13] Extracting a useful signal from InSAR data can be difficult due to complications introduced by dense vegetation or snow that shields the land surface, DEM and orbital errors, a weak deformation signal, and atmospheric interference [*Wright et al.*, 2004]. Furthermore, non-tectonic causes of surface-elevation change like subsidence due to either reduced runoff or groundwater extraction [e.g., *Bawden et al.*, 2001] can complicate the interpretation of interferometric data. If groundwater flow is controlled by fault planes, a spurious coincidence between structures and surface deformation may arise. A combination of careful selection of raw data used to generate interferograms and fortuitous geography allow for the visualization of the pattern of interseismic deformation across the Naryn Basin. The basin and surrounding ranges lie in an arid region with little vegetation other than sparse grasses. Some valley bottoms support agriculture, and these regions do not provide a coherent InSAR signal. We use synthetic aperture radar (SAR) data acquired from the European Space Agency's ENVISAT satellite platform, which generally has more reliable measurements of orbit parameters compared to the older European Remote-Sensing (ERS) platform. From this collection of archived images, we select those acquired between May and October when snow cover is unlikely. We only use image pairs with very short (<80 m) baseline separation between satellite acquisition positions (Table 1). This proximity minimizes the effects of DEM errors and rough topography on calculated range change. Atmospheric water vapor can affect the radar signal as it passes from the satellite to the land surface and back [*Li et al.*, 2005]. Because this region is arid and situated at elevations near 2000 m, these sources of error are, on average, likely small [*Wright et al.*, 2001].

[14] We use the standard processing steps of the ROI PAC software [*Rosen et al.*, 2004] to form six independent interferograms from 12 radar scenes acquired by the ENVISAT satellite on descending orbit 463 (Table 1). For each interferogram, these steps include: creation of complex-valued SAR images from the raw data, generation of the interferogram, orbital corrections, removal of the topographic signal based on the ASTER GDEM data set [*NASA and METI*, 2009], and phase unwrapping. Topographic correction using the lower-resolution SRTM elevation data set produced similar results, except over some areas of rough topography. Five of the six interferograms were averaged, with each weighted according to its time span, and then masked to remove areas not covered by interferograms spanning an aggregate of at least 9 years. Because the sixth interferogram displayed much higher, widespread, and unrealistic rates of range change (~20 mm/y), which we attribute to atmospheric delays, it was not used for analysis. The resultant stacked InSAR image shows relative rates of change in line-of-sight (LOS) distance across the basin (Figure 4).

3.2. Balanced Cross-Sections

[15] Movement on faults within the basin has deformed both overlying strata and geomorphic features such as river terraces. Because the geometry of faults underlying the Naryn Basin modulates the pattern of deformation observed at the surface, measurements of the overlying deformed strata and unconformities place useful constraints on the location and orientation of the faults, as well as the magnitude of slip along them. We supplement our own structural measurements (n = 324) with those of *Omuraliev* [1988] (n = 12) and *McLean* [1999] (n = 34). A series of five balanced cross-sections illustrate an admissible description of faults within the basin (Figure 5). (Maps are available as auxiliary material.) Each cross-section is area balanced and retrodeformable using a combination of fault-parallel flow and trishear-folding algorithms in the *2DMove* software program.

[16] In addition to bedding attitudes, the balanced cross-sections are constrained by several other considerations. First, where a single structure is transected by multiple cross-sections, the orientation of the underlying fault is held constant. Second, the absence of basal Kokturpak or Shamsi Formation in exposures across many structures limits the structural relief of these structures. For example, in section A-A′, these bright red units are not exposed above the south-dipping fault system (A2 in Figure 5). Their absence

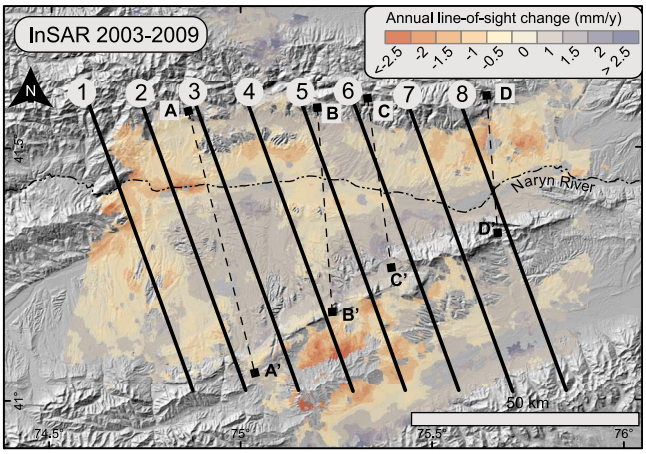

Figure 4. Satellite line-of-sight range change determined from five stacked InSAR images spanning from 10/18/2003 to 6/13/2009. Negative (red) values represent decreased line-of-site distance, similar to uplift. Regions with no data are either outside of the SAR scene acquisition, or lost coherence between repeat acquisitions. Topographic and deformational swath profiles 1 through 8 are shown in Figure 9. Lines A-A′ through D-D′ mark cross-section locations in Figure 5.

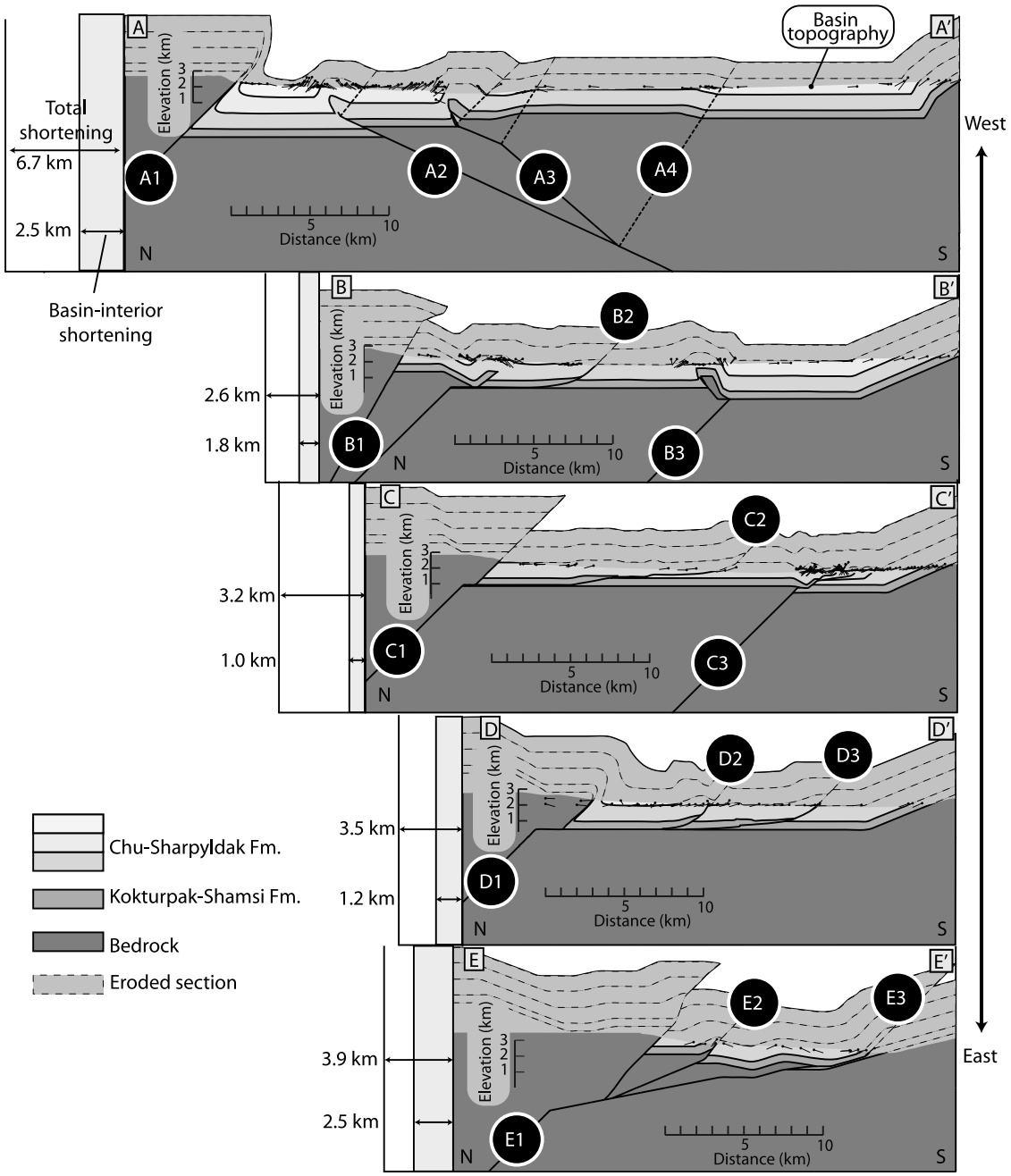

Figure 5. Five cross-sections across the Naryn Basin show the change in structural style along the east-west length of the basin (see Figure 2 for cross-section location). To the east, deformation of the basin interior is related to low-angle splays of the northern basin-bounding fault. To the west, deformation commonly occurs above reverse faults with no detachment linked to the basin margin.

limits the amount of slip that these structures may have accommodated.

[17] Deformed fluvial terraces provide additional constraints on fault geometry. In the eastern sections, D-D′ and E-E′, abandoned river-cut terraces that formed nearly perpendicular to fault traces have subsequently been faulted and folded. If the exposed fault had a constant dip in the subsurface, the terrace preserved in the hanging wall would be expected to be uniformly uplifted. Instead, the observed vertical displacement of the terrace in the hanging wall decreases away from the fault. We, therefore, infer a decrease in fault dip at depth from this terrace geometry [*Amos et al.*, 2007; *Thompson et al.*, 2002].

4. Results

4.1. Balanced Cross-Sections

[18] Making balanced sections in the absence of subsurface data is fraught with uncertainties. Even though careful mapping across the basin constrains surface dips, and deformed geomorphic markers are sometimes indicative of a specific fault geometry, the balanced cross-sections

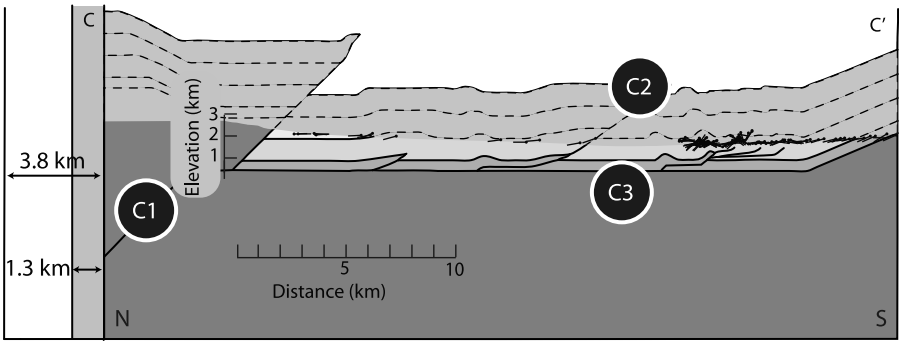

Figure 6. Alternative balanced cross-sections along C-C′. The observed bedding deformation pattern is compatible with the presence of either a basin interior reverse fault (C3 in Figure 5) or a detachment linked to the basin-margin fault (C3).

(Figures 5 and 6) represent only one of many subsurface fault geometries that could be compatible with these data. For example, the western section, A-A′ (Figure 5), illustrates that the basin-interior anticlines in western Naryn Basin could result from slip on a pair of linked south-dipping faults, but an equally valid interpretation would invoke two separate, more steeply dipping faults.

[19] Folding of the north limbs of the observed anticlines is attributed to steepening above buried fault tips. Indeed, where multiple fluvial terraces are preserved across the northern limb of the central anticline (A3 in Figure 5), older surfaces show steeper dip than younger surfaces implying progressive steepening of the northern fold limb. In contrast, farther south along section A-A′, fluvial terraces and underlying strata record advection into the south-dipping fold limb across an axial surface (A4 in Figure 5) as predicted above a fault bend (Figure 7a). Based on this interpretation, the observed fold-scarp dip of ~20° of the south limb and an assumed 45° dip on the causative fault below the fault bend would imply an increase in fault dip across the fault bend >45° [*Chen et al.*, 2007b]. Because the buried reverse fault is unlikely to have a near vertical dip above the fault bend, the dip of the causative fault at depth is likely to be less than 45°. The gentler fault dip of 25° (A3 in Figure 5) at depth also allows for sufficient slip to account for the magnitude of folding visible at the surface without requiring that the red basal (Shamsi) units be exposed in the cores of the anticlines where they are not observed. The northern range-bounding fault (A1 in Figure 5) is assumed to dip to the north at 45°, similar to the active faults that rupture through the brittle crust to the north [*Mellors et al.*, 1997]. The minimum amount of slip on this range-bounding fault, which may represent a family of range-front structures, is constrained only by the elevation of the adjacent range.

[20] Farther east, section B-B′ transects a box-shaped anticline in the basin interior (B2 in Figure 5). Twenty kilometers along strike, section C-C′ crosses the lateral continuation of this structure (Figure 2) where it is cut by a suite north-dipping thrust faults (C2). We assume that both the exposed faults and the broad anticline are the surface expression of the same north-dipping fault system illustrated in sections B-B′ and C-C′ as faults B3 and C3, respectively. Neither bedding attitudes nor deformed surfaces are preserved immediately north of this structure due to the presence of the modern Naryn River floodplain. Without such data to constrain the balanced cross-section along C-C′, it is possible to draw an admissible section showing the underlying fault as dipping at 45° beneath the basin interior (Figure 5) or linked to the range-front fault system by a gentle detachment (Figure 6). Based on the surface InSAR deformation pattern (discussed later), the reverse fault interpretation is preferred over the low-angle thrust interpretation.

[21] North of the Naryn River, sections B and C also share a similar pattern of gentle folding that is attributed to splays of the northern range-front fault (B2 and C2). These faults are not exposed at the surface, and may be buried

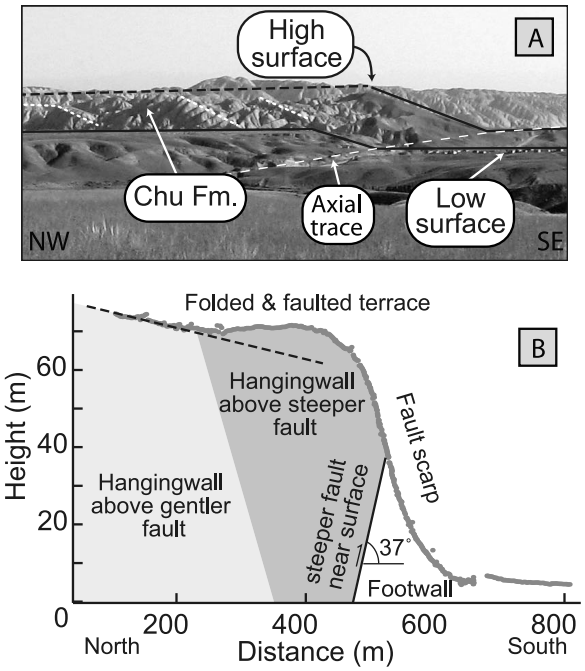

Figure 7. (a) Deformed fluvial terraces and strata across the axial surface A4 in Figure 5. Progressive lengthening of the fold limb is interpreted to indicate advection of material across a fault bend. (b) Differential GPS survey of folded and faulted terrace across fault D2 in Figure 5. Northward tilting of the hanging wall terrace implies a decrease in fault dip at depth.

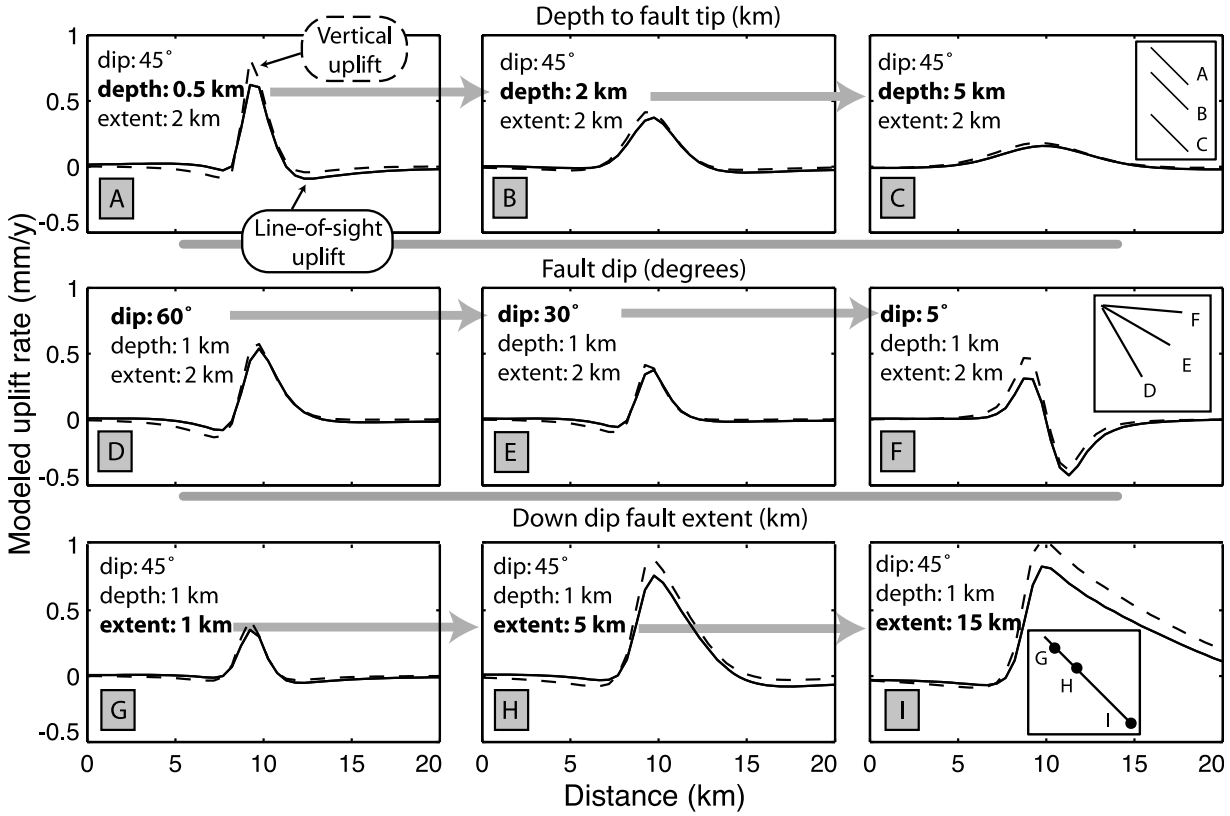

Figure 8. Model results showing predicted InSAR signal (solid curve) and predicted vertical uplift rate (dashed curve) caused by 2 mm/y of slip on faults within an elastic half-space (Poisson's ratio = 0.25, Young modulus = $8 \cdot 10^5$ bar). Faults have a strike of 60° and dip to the southeast. Rates are predicted along a line with a 150° trend. Curves illustrate the effect of (a–c) varying the depth to the fault tip, (d–f) varying fault dip, and (g–i) varying the downdip extent of the fault. Inset diagrams in Figures 8c, 8f, and 8g illustrate fault geometries used in each set of model realizations.

beneath the Naryn River floodplain as the sections illustrate. This interpretation is supported by the presence of north-dipping faults (D2, D3, and E3) that are unambiguously exposed in sections D-D′ and E-E′ along strike from the folds in sections B-B′ and C-C′.

[22] Sections D and E are similar to each other in that all of the basin-interior deformation is attributed to splays of the range-front fault. Exposed, north-dipping faults cut abandoned fluvial terraces in the basin interior along both eastern sections. The folding of terraces in the hanging walls indicates that fault dip decreases at depth (Figure 7b). One prominent difference between sections D and E is that the red stratigraphic units that represent the Kokturpak and Shamsi formations are only exposed in the hanging walls of faults in the easternmost section.

4.2. Comparison of InSAR and Balanced Cross-Sections

[23] Interseismic deformation at the surface is commonly modeled assuming that the crust is elastic and may be deformed by slip on fault patches contained within the otherwise homogenous medium [*Bürgmann et al.*, 1998; *Cakir et al.*, 2005]. Even though the basin stratigraphy argues against true homogeneity, and we lack a three-dimensional measure of surface velocity, we use such an elastic model to guide our interpretation. We use the *Coulomb* 3.2 software [*Lin and Stein*, 2004; *Toda et al.*, 2005] to predict 3-dimensional surface deformation patterns resulting from slip on dislocations, or faults, buried within an elastic medium representing the crust. The calculated surface displacements are converted to satellite line-of-sight (LOS) predictions and compared to our InSAR measurements in order to evaluate whether the measurements are compatible with the structural interpretation presented in the cross-sections. These model results demonstrate several salient characteristics (Figure 8). First, slip on deeper fault patches leads to uplift that is both less and distributed across a broader region than slip accommodated near the surface: the latter causes greater uplift across a smaller area (Figures 8a–8c). Second, more gently dipping faults create less surface uplift and can even cause marked subsidence, rather than ubiquitous uplift (Figures 8d–8f). If the same amount of slip is spread over a fault patch that extends deeper into the modeled crust, the magnitude and wavelength of uplift increases (Figures 8g–8i). Finally, were shortening accommodated only along a detachment at the base of the brittle crust (~17 km) without slip on shallower fault patches, the resultant broad warp of the ground surface would probably not be seen in the InSAR signal, because such long-wavelength features are removed during InSAR processing.

[24] A series of swath profiles from the InSAR data (Figure 4) with 10-km spacing along the basin reveals a transition in modern deformation patterns from west to east

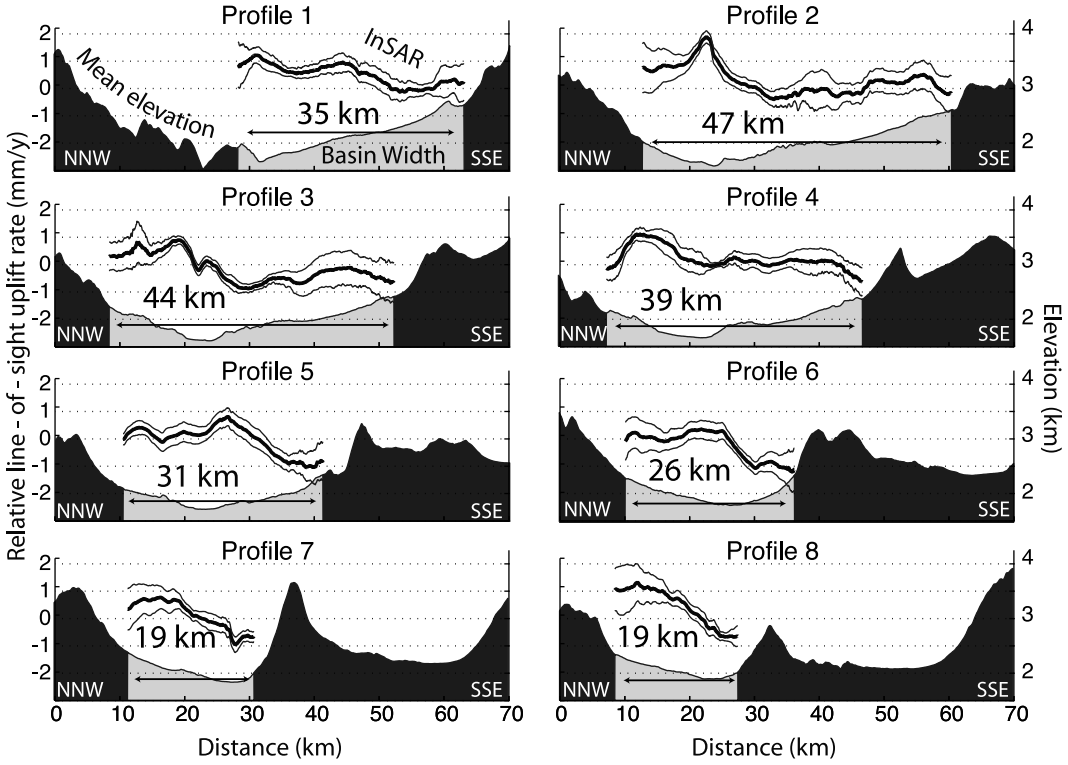

Figure 9. Average rates of InSAR line-of-sight range-change along a series of 10-km-wide swaths oriented at 150°, perpendicular to the strike of many basin-interior structures (see Figure 4 for profile locations). Mean rates are shown with 1 standard error bounds. Average elevation is shown along the same swaths. Gray fill shows where Cenozoic strata underlie topography. Basin width is measured between the outcrops of Paleozoic bedrock. Western swaths (1–6) show deformation distributed within the basin interior. Eastern swaths (7–8) show deformation concentrated at the northern range front.

that is compatible with the changes in underlying fault geometry (Figure 9). Swath profiles are oriented along 150°, perpendicular to the dominant strike direction of basin-interior structures and roughly parallel to the dominant p-axis orientation derived from regional earthquake focal mechanisms [*Ghose et al.*, 1998]. Across each 10-km-wide swath, average deformation rates, $\overline{U}(x)$, are calculated at each position, x, along the profile by: (1) calculating the average cross-swath line-of-sight rate, $\overline{u}_i(x)$, along a profile in each individual interferogram (i); (2) weighting the data along each profile by the time span, t_i, of the interferogram and dividing by the summed time spans of the five interferograms,

$$\overline{U}(x) = \frac{\sum_i \overline{u}_i(x) \cdot t_i}{\sum_i t_i}. \quad (1)$$

[25] The uncertainty envelope (Figure 9) represents the standard error of each point along the weighted mean profile, $s(x)$, calculated from the weighted variance, $s_w^2(x)$, among n individual interferogram profiles:

$$s(x) = \frac{\sqrt{s_w^2}}{n-1}. \quad (2)$$

[26] This unbiased estimate of the error describes how tightly the 5 individual interferograms constrain the mean swath profile, in contrast to the weighted standard deviation, which would describe how broadly the individual profiles were distributed about the mean profile.

[27] The orientation and depth of faults cutting the basin interior are not tightly constrained by the mapping of structures at the surface. Quantitative comparison between InSAR rates and modeled displacement fields, however, typically assumes a precise fault geometry and adjusts the fault slip rate on this assumed fault system, such that the modeled displacement matches the observed signal. Given the uncertainty associated with our interpretation of structures at depth, and the likelihood that the orientation of the faults changes along strike, this typical approach is unwarranted in the Naryn Basin, where detailed subsurface data are lacking. Instead, we demonstrate that slip on a simplified version of the interpreted fault geometry is generally compatible with the observed InSAR signal across the basin.

[28] Profile 3 most closely transects the structures illustrated in cross-section A-A′ (Figure 5). Farther west, profiles 1 and 2 are similar to profile 3 in that they generally show a pattern of increasing uplift (decreasing LOS distance) from south to north, a peak in deformation 5–10 km from the northern basin margin, and a decrease in uplift farther north. The surface deformation pattern predicted above a south-dipping fault system simplified from cross-section A-A′ generally agrees with the observed InSAR signal along profile 3 (Figure 10a). Based on the similarity between the observed and modeled deformation patterns,

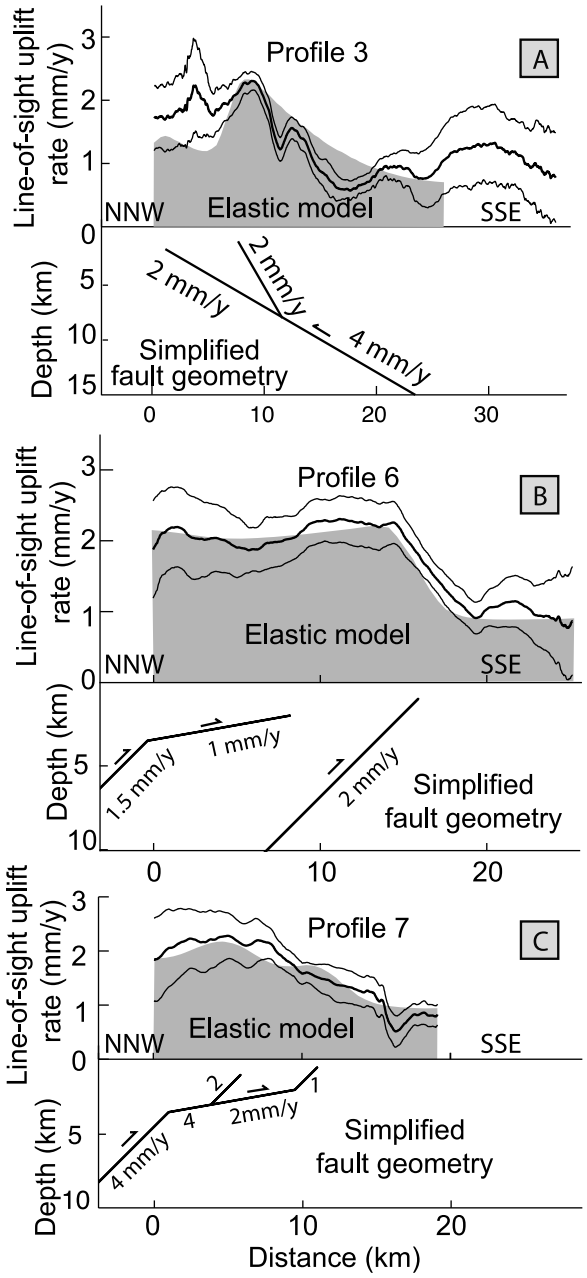

Figure 10. Predicted InSAR signals along a line trending at 150° that lies (a) above a southeast-dipping fault bend with strike of 60° and (b and c) above north-dipping fault systems with strikes of 270°. In Figure 10a, the fault-bend model is a simplified representation of the structures in the western Naryn Basin shown in cross-section A-A′ (Figure 5). In Figure 10b, the model for profile 6 is based on the fault geometry shown in cross-section B-B′ (Figure 5). In Figure 10c, the detachment model represents the detachment fault geometry of the eastern Naryn Basin shown in cross-section D-D′ (Figure 5).

we suggest that interseismic creep on the fault system marked A2 and A3 in cross-section A-A′ (Figure 5) is largely responsible for the InSAR signal in profiles 3. West of profile 3, the along-strike continuation of the south-dipping faults in cross-section A-A′ may be responsible for the surface deformation patterns observed along profiles 1 and 2.

[29] Profiles 5 and 6 transect the structures illustrated cross-sections B-B′ and C-C′. Each profile shows gradually increasing uplift rates from south to north followed by a steady or moderately decreasing rate at a distance of 15–20 km from the northern range margin. The observed 15-km-wide zone of near uniform uplift across the northern part of the transects is not consistent with uniform slip along a gently dipping, shallow detachment fault, which produces substantial uplift only near the fault tip line. Thus, the structural interpretation showing a steeply dipping, basin-interior fault (C3, Figure 5) is preferred over a detachment fault interpretation (Figure 6). Interseismic slip along a simplified version of the faults presented in cross-section C-C′ (Figure 5) can closely match (Figure 10b) the observed InSAR signal along the adjacent profile 6. Profile 4 falls in the transition zone between the south-dipping faults illustrated in A-A′ and north-dipping fault in B-B′. The InSAR signal from profile 4 bears greater similarity to profiles 3 than to profiles 5 and 6 suggesting that south-dipping structures as shown in section A-A′ may absorb most of the deformation at this location.

[30] Profiles 7 and 8 show the most rapid uplift at the northern edge of the basin and uplift rates that decrease to the south. The fault geometry in cross-section D-D′ (Figure 5) suggests that this eastern part of the basin is deformed by two faults that link along a gentle detachment surface to the steeper basin-margin fault. A simplified version of this geometry can predict an InSAR signal that shows a similar decrease in uplift rates from north to south as the magnitude of interseismic slip diminishes along the detachment system (Figure 10c).

[31] Each of the three elastic models (Figure 10) used to reproduce the observed InSAR signals across the basin requires that the modeled faults across the basin accommodate 3.5–4 mm/y of slip. Creep of this magnitude could account for ~70% of the 3–4 mm/y of horizontal shortening observed across the Naryn Basin with campaign GPS studies [*Zubovich et al.*, 2010].

5. Discussion

[32] Because many atmospheric effects and non-tectonic changes in the ground surface could be misinterpreted as a tectonic signal, it is difficult to evaluate how faithfully the InSAR data across the Naryn Basin (Figures 4 and 8) record activity on faults. Two independent measures of modern tectonic deformation within the basin support our interpretation that the InSAR signal is largely tectonic. Typical InSAR deformation rates across the basin fall within the range of −2 to +2 mm/yr (Figure 5) and are consistent with those from a published level-line survey that yielded point measurements of vertical deformation rates between −1.2 and +1.9 mm/yr [*Tsurkov*, 1986]. Furthermore, the near-vertical InSAR rates are reasonable when compared with horizontal GPS velocities from the Naryn region showing 3–4 mm/y of north-south shortening [*Zubovich et al.*, 2010].

[33] Comparisons between the InSAR signal (Figure 4) and balanced cross-sections (Figure 5) address some of the ambiguities of each data set. The spatial coincidence of active structures measured in the field and pronounced line-of-sight InSAR range change supports our conclusion that much of the InSAR signal is tectonically derived. Conversely, surface deformation patterns observed in the InSAR can indicate

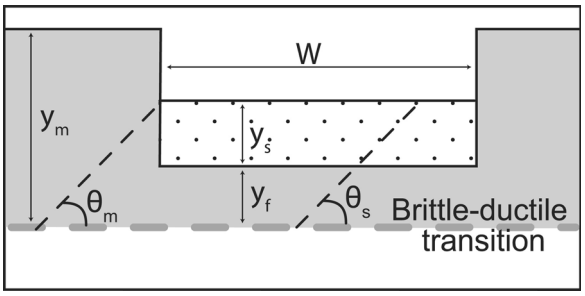

Figure 11. Illustration of mechanical model setup. Faults (black dashed lines) dip at angles of θ_m from the range-front and of θ_s from the basin interior through the brittle crust. Stress required to activate each fault is calculated based on the effective lithostatic stress across the fault plane at the base of the brittle crust, as calculated from the thickness of the range y_m above the basal segment of the fault or the thickness of the pre-Cenozoic bedrock, y_f, and the overlying basin fill, y_s.

which one of alternative structural interpretations is more likely, resulting in a better-constrained cross-section.

[34] Although the deformation patterns recorded by long-term deformation of basin-filling strata shown in cross-sections and InSAR represent vastly different time scales, they are consistent with each other across parts of the Naryn Basin. The similarity between the long (10^5 y) and short-term (10^1 y) deformation patterns encourages us to interpret the InSAR deformation signal as resulting from interseismic creep along some active faults.

[35] The western InSAR profiles of surface deformation (profiles 1–6: Figure 9) show that recent uplift is distributed within the basin interior. Although the locus of greatest uplift appears to shift across the western basin interior, it is never concentrated at the basin margin as it is in the eastern profiles (profiles 7–8: Figure 9), which show greatest uplift near the northern range front. Thus, we infer that the western Naryn Basin reveals a pattern of fault activity in which the long-lived basin-margin fault has become inactive in favor of faults in the basin interior. We investigate controls on basin-interior faults with a simple mechanical model that accounts for range topography and basin geometry.

6. Geomechanical Model of Basin-Interior Faulting

[36] So-called "wedge" models of orogen-scale faulting typically assume a continuously sloping range front, an arbitrarily wide foreland into which thrust faults may propagate, and uniform density throughout the crust [*Dahlen et al.*, 1984; *Hilley et al.*, 2005]. As a consequence of these assumptions, these models are not well suited to exploring the controls on faulting in basins formed in the interior of contractional orogens. In contrast to such wedge models, the Naryn Basin is characterized by several kilometers of basin-filling strata with lower density than the surrounding ranges, a finite width, and an abrupt transition in elevation from the basin floor to ranges rising abruptly 1–2 km above the basin fill.

[37] We apply a simple geo-mechanical model (Figure 11) to predict the conditions under which hypothetical structures that cut the basin interior are more likely to be activated than those structures that define the basin margins. The horizontal tectonic stress, σ_{xm}, required to initiate failure of a basin-bounding fault and the tectonic stress, σ_{xs}, required to initiate failure on a basin interior fault are compared. The ratio of these quantities represents the favorability of the basin interior fault (F), or the factor by which the strength predicted for the basin-interior fault must be exceeded in order to activate the basin-margin fault instead of the basin-interior fault:

$$F = \frac{\sigma_{xm}}{\sigma_{xs}}. \tag{3}$$

[38] Following the mechanics proposed by *Anderson* [1951], the tectonic stress required for failure on a given reverse fault plane [*Turcotte and Schubert*, 1982] can be approximated as

$$\sigma_x = \frac{2\mu L}{\sin(2\theta) - \mu[1 - \cos(2\theta)]}. \tag{4}$$

[39] The horizontally directed stress required to cause failure on a fault plain σ_x depends on the fault dip θ, the coefficient of friction on the fault μ, and the effective lithostatic stress provided by the overlying column of rock L. The effective lithostatic stress assuming connectivity to the surface [*Hubbert and Rubey*, 1959] can be written in terms of the depth of the fault plane in question and material densities:

$$L = g\left[\sum\nolimits_i \rho_i y_i - \rho_{water} y_{total}\right]. \tag{5}$$

[40] The gravitational constant g, individual layer thickness y_i and density ρ_i contribute to the lithostatic stress. From equations (4) and (5), it is apparent that the tectonic stress required to activate a particular reverse fault increases monotonically with depth as the overburden increases. Because this description approximates the behavior of the brittle crust only, the strongest portion of a given fault is assumed to be near the base of the brittle crust where the overburden is greatest, but above the point where the crust loses its brittle properties due to increased temperature [*Sibson*, 1982]. Thus, fault favorability F is determined by comparing the tectonic stresses required to rupture the basin-interior and basin-bounding faults near the base of the brittle crust. The lithostatic component is, therefore, determined by the thickness and density of the column of rock that overlies a given fault plane near the brittle-ductile transition. Given the simplified basin geometry (Figure 11), the effective lithostatic stress experienced by a basin-margin fault at the base of the brittle layer L_m can be expressed as

$$L_m = \rho_m y_m - \rho_{water} y_m. \tag{6}$$

[41] The lithostatic load experienced by a basin-interior fault L_s is dependent on whether or not the basin has sufficient width w for the fault to cut the entire brittle crust without dipping below the basin margin:

$$L_s = \rho_m y_f + \rho_s y_s - \rho_{water}\left(y_f + y_s\right) \quad \text{for} \quad w \geq \left(y_s + y_f\right)/\tan(\theta_s) \tag{7a}$$

$$L_s = L_m \quad \text{for} \quad w < \left(y_s + y_f\right)/\tan(\theta_s). \tag{7b}$$

Table 2. Basin Model Parameters

Parameter (symbol)	Value	Source
Bedrock relief	5.5 km	*Cobbold et al.* [1996]
Dip of fault (θ_m, θ_s)	45°	*Mellors et al.* [1997]
Density of bedrock (ρ_m)	2700 kg/m^3	*Yudakhin* [1986]
Density of basin sediment (ρ_s)	2300 kg/m^3	*Yudakhin* [1986]
Coefficient of friction (μ)	0.85	*Byerlee* [1978]
Depth of brittle-ductile transition below basin	17 km	*Mellors et al.* [1997]
Thickness of basin sediment (y_s)	3.5 km	*Omuraliev* [1978]

[42] Parameter values from the Central Tien Shan are used to constrain this model (Table 2). The brittle crust is approximately 17 km thick based on an aftershock study [*Mellors et al.*, 1997] consistent with the 15- to 20-km range reported for the North American crust [*Sibson*, 1982]. The density of the Naryn Basin fill and surrounding ranges is reported as 2340 kg/m^3 and 2670 kg/m^3 respectively [*Yudakhin*, 1986]. Measured stratigraphic sections in the Naryn Basin [*Omuraliev*, 1978] indicate that the basin-filling strata are at least 3.5 km thick (Figure 3). We specify that both modeled faults are planar, strike parallel to each other, have equivalent frictional properties, and extend from the surface to the base of the brittle crust.

[43] First, we consider how variations in basin width could affect the favorability of a basin-interior fault with the same orientation as a range-bounding fault (Figure 12a). In a narrow basin (<17 km wide for a 45°-dipping fault), the "favorability" is 1, meaning that a basin-interior fault would require the same tectonic stress to become active as the extant basin-margin fault (Figure 11a). Even though the fault daylights in the basin interior, its lower extent dips below the basin-bounding topography before reaching the base of the brittle crust. In a wide basin (>17 km for a 45°-dipping fault), the "favorability" of the basin-interior fault is greater than 1, thereby indicating that such a fault would be more likely to slip than the basin-margin structure. The critical width of 17 km that defines the abrupt shift in fault favorability is simply the minimum basin width that would allow for a 45°-dipping fault to cut the entire, 17-km-thick brittle crust without dipping below the load of the basin-bounding topography.

[44] The comparison between basin-margin and basin-interior fault strength is dependent on the orientations and locations of faults deep below the surface. One weakness of this approach is that these parameters are poorly constrained by data from the Naryn Basin. Additionally, we have assumed that stresses acting on the fault plane above the base of the brittle layer are irrelevant to the strength of the fault. We do not consider the work required to lift the overlying topography along the fault plane [*Masek and Duncan*, 1998] or to generate new faults. Although the presence of range-bounding topography above the fault at depth could be a real control on fault strength, the step-like shift in favorability at precisely 17 km width is an artifact of this simple model setup. Two considerations indicate that this step in favorability is likely to be a more gradual transition in reality. First, the range does not rise vertically from the basin margin. Rather the range front has a slope of about 20°. Second, the denser rocks of the range have likely been thrust over lower-density basin fill at the range margin as illustrated in the cross-sections and imaged geophysically in a nearby basin [*Park et al.*, 2003]. The lack of either a step change in density or elevation at the range margin indicates that the step-like change in favorability could be better described by a broader transition from low to higher favorability of basin-interior faults with increasing basin width. Additionally, this analysis assumes that inherited faults with similar orientation to the range-front fault cut the basin interior. This assumption is perhaps not unreasonable given that the region experienced early orogenic events that predate the formation of the modern Tien Shan [*Burtman*, 1975; *Sengör and Natal'in*, 1996; *Windley et al.*, 2007]. Numerous minor faults and fractures are evident within the Paleozoic bedrock where the unconformity surface has been exposed on the flanks of the southern basin-bounding range (Figure 13). If similar zones of weakness cut the bedrock beneath the basin, they represent potential slip surfaces that could guide patterns of active faulting.

[45] Despite these caveats regarding the modeled step in topography and density at the basin margin, the 30-to-40-km-wide western Naryn Basin is sufficiently wide to contain 45°-dipping, basin-interior faults that do not dip below the surrounding ranges. Cross-section A-A′ in the wide western Naryn Basin suggests that basin-interior faults

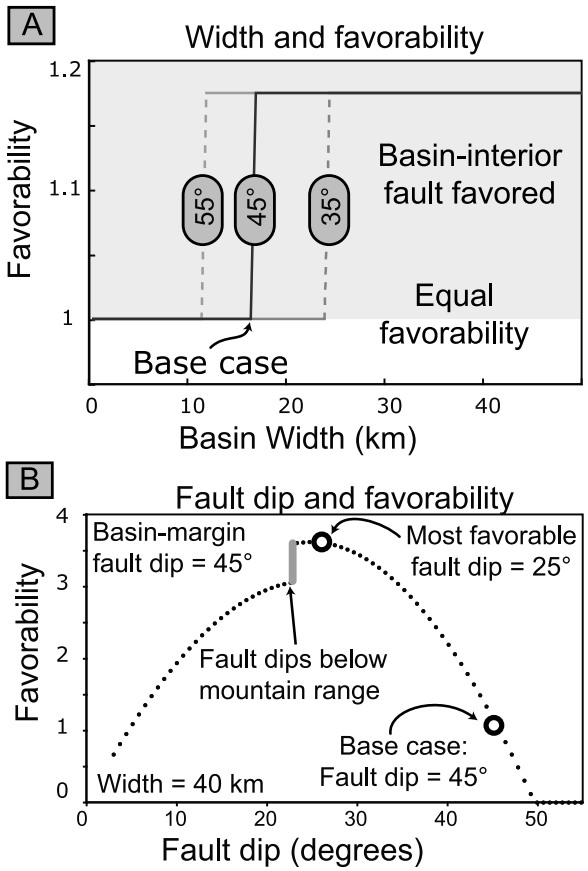

Figure 12. (a) Model results show an increase in favorability of basin-interior faults in a wide basin assuming parallel, basin-interior and basin-margin faults with dips of 55°, 45°, and 35°. (b) Changes in basin-interior fault favorability with varying dip of basin-interior fault and 45° dip of basin-margin fault demonstrated with a 40-km-wide basin.

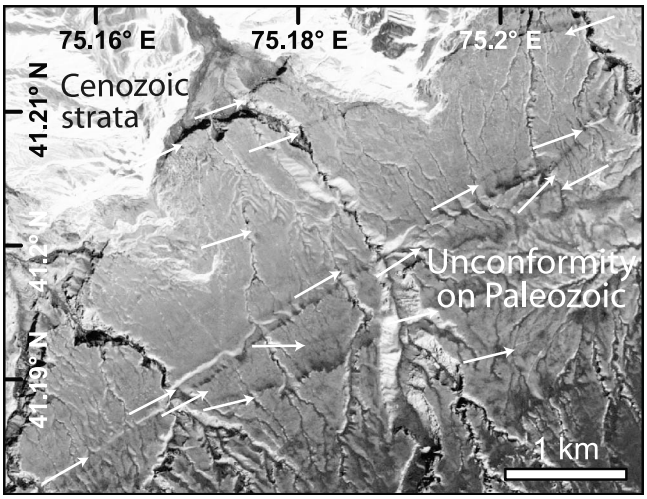

Figure 13. SPOT satellite image showing the unconformity surface where basin-filling units have been stripped from the north flank of the southern basin-bounding Baybeiche range (for location, see star, Figure 2). Arrows indicate the many minor faults and fractures breaking the surface.

with dips gentler than the range-front fault are also active. Indeed, faults with gentler dips could form in such a wide basin without experiencing increased topographic overburden. As fault dip decreases from the 45° assumed in the base case, the basin-interior structure becomes weaker as calculated by equations (3)–(5) and is thus more favorable up to a peak in favorability at 25° (Figure 11b). This prediction demonstrates one of the classic results of 'Andersonian' fault mechanics: the most favorable orientation for thrust-fault formation is generally at about 25° with some variation depending on the frictional coefficient. At gentler dips in our model, the favorability begins to decrease gradually before experiencing an abrupt drop in favorability (Figure 11b). This abrupt decrease in favorability at a 23° dip represents the angle at which a basin-interior fault would dip below the basin-bounding range.

[46] Based on this model, the wider western Naryn Basin favors the activation of basin-interior faults, whereas the narrower eastern Naryn Basin favors the continued activity of the range-front fault system. If a reverse fault were located in the narrow eastern basin, the fault plane would dip below the adjacent range. In this scenario, the new fault would experience nearly the same topographic load as the extant range-front fault. As a result, the model predicts that basin-interior faults within the narrow part of the basin would not be favored over range-front faults. To the west, a steeply dipping, basin-interior fault could extend many kilometers below the surface without passing beneath the topographic load of the surrounding ranges (Figure 14). Furthermore, faults with gentler dip could be active in the widest part of the basin without dipping below the ranges. This interpretation is supported by both balanced cross-sections and InSAR-derived surface deformation patterns. These lines of evidence each indicate that the wide western Naryn Basin is likely to be deformed by reverse faults that do not link to the basin-bounding fault system at depth. In contrast, the pattern of faulting and surface deformation in the narrow part of the basin to the east is more consistent with low-angle splays emanating from the existing basin-bounding fault system.

[47] The balanced cross-sections (Figure 5) show three faults that cut the basin interior without linking to the basin-bounding fault system. In section A-A′, the south-dipping basin interior fault (A2) would reach a depth of 18 km before passing beneath the southern range. Similarly in sections B-B′ and C-C′, the north-dipping basin interior fault system (B3 and C3) would reach a depth of 20–23 km before passing beneath the northern range. Although these faults do not in reality have an infinite downdip extent, these calculations demonstrate that the basin-interior faults within the brittle crust (~17 km), as illustrated in the cross-sections, are unlikely to experience enhanced topographic loading from the surrounding ranges.

7. Conclusions

[48] This study presents a suite of balanced cross-sections that represent the first numerically balanced sections across the actively deforming Naryn Basin in south-central Kyrgyzstan. Although previous studies found evidence of basin deformation linked only to basin-margin fault systems in multiple basins across the Tien Shan [*Abdrakhmatov et al.*, 2001; *Park et al.*, 2003; *Thompson et al.*, 2002], these new cross-sections across the Naryn Basin show that basin-interior structures may be independent of the basin-margin fault system in the western part of the basin.

[49] The cross-sections show 3–7 km of shortening, but these values are only loosely defined because the total uplift of the northern basin-bounding range is constrained only loosely by the range elevation and because the dip of the basin-bounding faults is uncertain. Nonetheless, this estimate is similar to the estimated 5–10 km of shortening across the Naryn Basin proposed on the basis of a reconstruction the regional unconformity surface [*Abdrakhmatov et al.*, 2001]. Despite relatively rapid geodetic and latest Quaternary shortening across the Naryn Basin at 3–4 mm/y

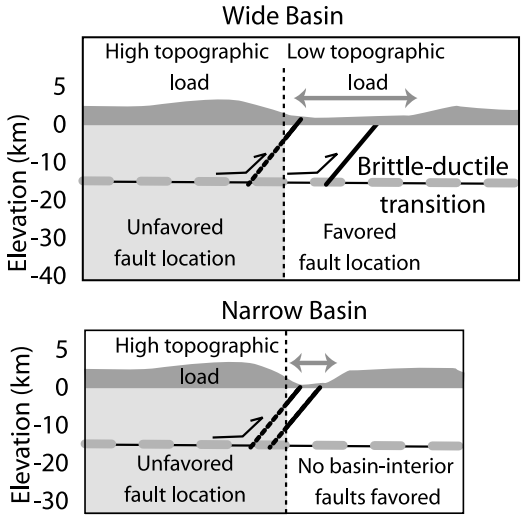

Figure 14. Illustration of range-bounding and basin-interior faults experiencing either high or low topographic loads depending on whether the lower extent of the fault dips below the heavier loads imposed by the range topography.

[*Thompson et al.*, 2002; *Zubovich et al.*, 2010], the cross-sections suggest that the basin interior has absorbed only 1–2.5 km of shortening. Thus, all of the basin-interior deformation may be less than 1 My old, assuming that past rates match modern geodetic rates and that basin-interior structures have accommodated most of the Quaternary shortening. Although the deformation rates from InSAR across the basin are insufficient to tightly define the underlying fault geometry and patterns of interseismic slip on them, a simple exploration of surface deformation caused by faults within an elastic half-space indicates that the observed deformation patterns are compatible with the structural interpretations illustrated in the cross-sections. Additionally, this modeling of surface displacements in an elastic half-space suggests that more than half of the shortening across the basin measured from GPS networks may be accommodated by creep on faults in the upper 17 km of the crust. In future research, seismic monitoring of microseismicity across the region may lend support to this finding.

[50] A first-order observation from the InSAR analysis is that modern uplift is focused near the basin margin where the basin is narrow, but is more distributed and commonly focused in the basin interior where the basin is wider. We make simple calculations of the stress acting on a fault plane assuming that the deepest part of the fault within the brittle crust is the strongest and that this strength controls whether or not a fault will slip. These calculations indicate that a wide basin may favor basin-interior fault activation provided that the fault does not dip below the surrounding high topography (Figure 14). This result would be most applicable to regions like the Tien Shan where pre-existing planes of weakness in the subsurface may guide active structures. In the absence of such pre-existing structures and despite the presence of high topography and a wide basin, established basin-bounding faults might remain active as a result of the additional tectonic stress required to initiate new faults in basin interiors. Even where intramontane basins have been filled by sediment such that substantial relief between a basin and surrounding ranges is absent, contrasts in density between bedrock ranges and basin fill may still favor faults within wide basins.

[51] **Acknowledgments.** We appreciate the patient assistance with InSAR and elastic modeling from Chen Ji. Cholponbek Ormukov, Kanatbek Abdrakhmatov, and Mirlan Dayirov provided valuable guidance in the field. We gratefully acknowledge NASA (NNX08AG05G) and the National Geographic Society Committee for Research and Exploration (8685-09) for funding this research. SAR data are provided in the frame of ESA Cat-1 project 3618. Interferograms are computed with the ROI_PAC open source software developed at JPL/Caltech. We thank Julien Charreau and an anonymous reviewer for thoughtfully reviewing earlier versions of this work.

References

Abdrakhmatov, K. Y. (1988), *Quaternary Tectonics of the Chu Basin*, Ilim, Bishkek, Kyrgyzstan.

Abdrakhmatov, K. Y., et al. (1996), Relatively recent construction of the Tien Shan inferred from GPS measurements of present-day crustal deformation rates, *Nature*, *384*, 450–453, doi:10.1038/384450a0.

Abdrakhmatov, K. Y., R. Weldon, S. C. Thompson, D. W. Burbank, C. Rubin, M. Miller, and P. Molnar (2001), Origin, direction, and rate of modern compression in the central Tien Shan, Kyrgyzstan, *Geol. Geofiz.*, *42*, 1585–1609.

Amos, C. B., D. W. Burbank, D. Nobes, and S. A. L. Read (2007), Geomorphic constraints on listric thrust faulting: Implications for active deformation in the Mackenzie Basin, South Island, New Zealand, *J. Geophys. Res.*, *112*, B03S11, doi:10.1029/2006JB004291.

Anderson, E. M. (1951), *The Dynamics of Faulting and Dyke Formation, With Applications to Britain*, Oliver and Boyd, Edinburgh, U. K.

Avouac, J. P., P. Tapponnier, M. Bai, H. You, and G. Wang (1993), Active thrusting and folding along the northern Tien Shan and Late Cenozoic rotation of the Tarim relative to Dzungaria and Kazakhstan, *J. Geophys. Res.*, *98*(B4), 6755–6804, doi:10.1029/92JB01963.

Bawden, G. W., W. Thatcher, R. S. Stein, K. W. Hudnut, and G. Peltzer (2001), Tectonic contraction across Los Angeles after removal of groundwater pumping effects, *Nature*, *412*, 812–815, doi:10.1038/35090558.

Bullen, M. E., D. W. Burbank, and J. I. Garver (2003), Building the northern Tien Shan: Integrated thermal, structural, and topographic constraints, *J. Geol.*, *111*, 149–165, doi:10.1086/345840.

Burbank, D. W., J. K. McLean, M. E. Bullen, K. Y. Abdrakmatov, and M. G. Miller (1999), Partitioning of intermontane basins by thrust-related folding, Tien Shan, Kyrgyzstan, *Basin Res.*, *11*, 75–92, doi:10.1046/j.1365-2117.1999.00086.x.

Bürgmann, R., E. J. Fielding, and J. Sukhatme (1998), Slip along the Hayward fault, California, estimated from space-based synthetic aperture radar interferometry, *Geology*, *26*, 559–562, doi:10.1130/0091-7613(1998)026<0559:SATHFC>2.3.CO;2.

Bürgmann, R., G. Hilley, A. Ferretti, and F. Novali (2006), Resolving vertical tectonics in the San Francisco Bay Area from permanent scatterer InSAR and GPS analysis, *Geology*, *34*(3), 221–224, doi:10.1130/G22064.1.

Burtman, V. S. (1975), Structural geology of Variscan Tien Shan, USSR, *Am. J. Sci.*, *275-A*, 157–186.

Burtman, V. S., S. F. Skobelev, and P. Molnar (1996), Late Cenozoic slip on the Talas-Ferghana Fault, the Tien Shan, Central Asia, *Geol. Soc. Am. Bull.*, *108*(8), 1004–1021, doi:10.1130/0016-7606(1996)108<1004:LCSOTT>2.3.CO;2.

Byerlee, J. D. (1978), Friction of rocks, *Pure Appl. Geophys.*, *116*, 615–626, doi:10.1007/BF00876528.

Cakir, Z., A. M. Akoglu, S. Belabbes, S. Ergintav, and M. Meghraoui (2005), Creeping along the Ismetpasa section of the North Anatolian fault (Western Turkey): Rate and extent from InSAR, *Earth Planet. Sci. Lett.*, *238*(1–2), 225–234, doi:10.1016/j.epsl.2005.06.044.

Charreau, J., J.-P. Avouac, Y. Chen, S. Dominguez, and S. Gilder (2008), Miocene to present kinematics of fault-bend folding across the Huerguosi anticline, northern Tianshan (China), derived from structural, seismic, and magnetostratigraphic data, *Geology*, *36*(11), 871–874, doi:10.1130/G25073A.1.

Chediya, O. K. (1986), *Morphostructure and Neo-Tectonics of the Tien Shan*, Acad. Nauk Kyrgyz, Frunze, U.S.S.R.

Chen, J., R. Heermance, D. W. Burbank, K. M. Scharer, J. Miao, and C. Wang (2007a), Quantification of growth and lateral propagation of the Kashi anticline, southwest Chinese Tian Shan, *J. Geophys. Res.*, *112*, B03S16, doi:10.1029/2006JB004345.

Chen, Y.-G., K.-Y. Lai, Y.-H. Lee, J. Suppe, W.-S. Chen, Y.-N. N. Lin, Y. Wang, J.-H. Hung, and Y.-T. Kuo (2007b), Coseismic fold scarps and their kinematic behavior in the 1999 Chi-Chi earthquake Taiwan, *J. Geophys. Res.*, *112*, B03S02, doi:10.1029/2006JB004388.

Cobbold, P. R., P. Davy, D. Gapais, E. A. Rossello, E. Sadybaksov, J. C. Thomas, J. J. Tondji Biyo, and M. de Urreiztieta (1993), Sedimentary basins and crustal thickening, *Sediment. Geol.*, *86*, 77–89, doi:10.1016/0037-0738(93)90134-Q.

Cobbold, P. R., E. Sadybaksov, and J. C. Thomas (1996), Cenozoic transpression and basin development, Kyrghyz Tienshan, Central Asia, in *Geodynamic Evolution of Sedimentary Basins*, edited by F. Roure et al., pp. 181–202, Ed. Tech., Paris.

Daëron, M., J.-P. Avouac, and J. Charreau (2007), Modeling the shortening history of a fault tip fold using structural and geomorphic records of deformation, *J. Geophys. Res.*, *112*, B03S13, doi:10.1029/2006JB004460.

Dahlen, F. A., J. Suppe, and D. Davis (1984), Mechanics of fold-and-thrust belts and accretionary wedges: Cohesive Coulomb wedge theory, *J. Geophys. Res.*, *89*, 10,087–10,101, doi:10.1029/JB089iB12p10087.

Fielding, E. J., T. J. Wright, J. Muller, B. E. Parsons, and R. Walker (2004), Aseismic deformation of a fold-and-thrust belt imaged by synthetic aperture radar interferometry near Shahdad, southeast Iran, *Geology*, *32*(7), 577–580, doi:10.1130/G20452.1.

Ghose, S., R. J. Mellors, A. M. Korjenkov, M. W. Hamburger, T. L. Pavlis, G. L. Pavlis, M. Omuraliev, E. Mamyrov, and A. R. Muraliev (1997), The Ms = 7.3 1992 Suusamyr, Kyrgyzstan, earthquake in the Tien Shan: 2. Aftershock focal mechanisms and surface deformation, *Bull. Seismol. Soc. Am.*, *87*(1), 23–38.

Ghose, S., M. W. Hamburger, and C. J. Ammon (1998), Source parameters of moderate-sized earthquakes in the Tien Shan, central Asia from

regional moment tensor inversion, *Geophys. Res. Lett.*, *25*(16), 3181–3184, doi:10.1029/98GL02362.
Hilley, G., P. M. Blisniuk, and M. R. Strecker (2005), Mechanics and erosion of basement-cored uplift provinces, *J. Geophys. Res.*, *110*, B12409, doi:10.1029/2005JB003704.
Hubbert, M. K., and W. W. Rubey (1959), Role of fluid pressure in mechanics of overthrust faulting, I. Mechanics of fluid-filled porous solids and its application to overthrust faulting, *Geol. Soc. Am. Bull.*, *71*, 617–682.
Hubert-Ferrari, A., J. Suppe, R. Gonzalez-Mieres, and X. Wang (2007), Mechanisms of active folding of the landscape (southern Tian Shan, China), *J. Geophys. Res.*, *112*, B03S09, doi:10.1029/2006JB004362.
Korjenkov, A. M., I. E. Povolotskaya, and E. Mamyrov (2007), Morphologic expression of Quaternary deformation in the northwestern foothills of the Ysyk-Köl basin, Tien Shan, *Geotectonics*, *41*(2), 130–148, doi:10.1134/S0016852107020045.
Li, Z., J. Muller, P. Cross, and E. J. Fielding (2005), Interferometric synthetic aperture radar (InSAR) atmospheric correction: GPS, moderate resolution Imaging spectroradiometer (MODIS), and InSAR integration, *J. Geophys. Res.*, *110*, B03410, doi:10.1029/2004JB003446.
Lin, J., and R. S. Stein (2004), Stress triggering in thrust and subduction earthquakes and stress interaction between the southern San Andreas and nearby thrust and strike-slip faults, *J. Geophys. Res.*, *109*, B02303, doi:10.1029/2003JB002607.
Masek, J., and C. C. Duncan (1998), Minimum-work mountain building, *J. Geophys. Res.*, *103*, 907–917, doi:10.1029/97JB03213.
Massonnet, D., M. Rossi, C. Carmona, F. Adragna, G. Peltzer, K. Feigl, and T. Rabaute (1993), The displacement of the Landers earthquake mapped by radar interferometry, *Nature*, *364*, 138–142, doi:10.1038/364138a0.
McLean, J. K. (1999), Neogene shortening across Naryn and at Bashi basins, southern Kyrgyz Tien Shan, M. S. thesis, Cent. Wash. Univ., Ellensburg.
Mellors, R. J., F. L. Vernohn, G. L. Pavlis, G. A. Abers, M. W. Hamburger, S. Ghose, and B. Illiasov (1997), The Ms = 7.3 1992 Suusamyr, Kyrgyzstan earthquake: 1. Constraints on fault geometry and source parameters based on aftershocks and body wave modeling, *Bull. Seismol. Soc. Am.*, *87*, 11–22.
Molnar, P., and S. Ghose (2000), Seismic moments of major earthquakes and the rate of shortening across the Tien Shan, *Geophys. Res. Lett.*, *27*, 2377–2380, doi:10.1029/2000GL011637.
NASA and METI (2009), ASTER Global Digital Elevation Model, https://wist.echo.nasa.gov/wist-bin/api/ims.cgi?mode=MAINSRCH&JS=1, Jet Propulsion Lab., Calif. Inst. of Technol., NASA, Pasadena, Calif.
Omuraliev, M. (1978), Geology and tectonic features of the Cenozoic Alabuga-Naryn Basin (central Tien Shan), Ph.D. thesis, Inst. of Geophys. and Seismol., Acad. of Sci. of the Kirghiz SSR, Frunze, U.S.S.R.
Omuraliev, M. (1988), Geologic map of Cenozoic deposits Alabuga-Naryn Basin, scale 1:200,000.
Omuraliev, M., and A. Korzhenkov (1995), Morphostructural parameters and stress-deformation state of the medium of seismic zones of the Tien Shan, *Geotectonics, Engl. Transl.*, *29*(2), 172–179.
Park, S. K., S. C. Thompson, A. Rybin, V. Batalev, and R. Bielinski (2003), Structural constraints in neotectonic studies of thrust faults from the magnetotelluric method, Kochkor Basin, Kyrgyz Republic, *Tectonics*, *22*(2), 1013, doi:10.1029/2001TC001318.
Reigber, C., G. W. Michel, R. Galas, D. Angermann, J. Klotz, J. Y. Chen, A. Papschev, R. Arslanov, V. E. Tzurkov, and M. Ishanov (2001), New space geodetic constraints on the distribution of deformation in Central Asia, *Earth Planet. Sci. Lett.*, *191*, 157–165, doi:10.1016/S0012-821X(01)00414-9.
Rosen, P. A., S. Henley, G. Peltzer, and M. Simons (2004), Updated repeat orbit interferometry package released, *Eos Trans. AGU*, *85*(5), 47, doi:10.1029/2004EO050004.
Scharer, K., D. W. Burbank, J. Chen, and R. J. I. Weldon (2006), Kinematic models of fluvial terraces over active detachment folds: Constraints on the growth mechanism of the Kashi-Atushi fold system, Chinese Tian Shan, *Geol. Soc. Am. Bull.*, *118*, 1006–1021, doi:10.1130/B25835.1.
Sengör, A. M. C., and B. A. Natal'in (1996), Turkic-type orogeny and its role in the making of the continental crust, *Annu. Rev. Earth Planet. Sci.*, *24*(1), 263–337, doi:10.1146/annurev.earth.24.1.263.
Sibson, R. H. (1982), Fault zone models, heat flow, and the depth distribution of earthquakes in the continental crust of the United States, *Bull. Seismol. Soc. Am.*, *72*(1), 151–163.
Sobel, E. R. (2003), Formation of internally drained contractional basins by aridity-limited bedrock incision, *J. Geophys. Res.*, *108*(B7), 2344, doi:10.1029/2002JB001883.
Tapponnier, P., and P. Molnar (1979), Active faulting and Cenozoic tectonics of the Tien Shan, Mongolia, and Baykal regions, *J. Geophys. Res.*, *84*(B7), 3425–3459, doi:10.1029/JB084iB07p03425.
Thompson, S. C., R. Weldon, C. M. Rubin, K. Y. Abdrakhmatov, P. Molnar, and G. W. Berger (2002), Late Quaternary slip rates across the central Tien Shan, Kyrgyzstan, central Asia, *J. Geophys. Res.*, *107*(B9), 2203, doi:10.1029/2001JB000596.
Toda, S., R. S. Stein, K. Richards-Dinger, and S. B. Bozkurt (2005), Forecasting the evolution of seismicity in southern California: Animations built on earthquake stress transfer, *J. Geophys. Res.*, *110*, B05S16, doi:10.1029/2004JB003415.
Tsurkov, V. E. (1986), Modern vertical crustal movements: Geodetic data, in *Lithosphere of the Tien Shan*, edited by I. E. Gubin, 156 pp., Nauka, Moscow.
Turcotte, D. L., and G. Schubert (1982), *Geodynamics Applications of Continuum Physics to Geological Problems*, John Wiley, New York.
Windley, B. F., D. Alexeiev, W. Xiao, A. Kroner, and G. Badarch (2007), Tectonic models for accretion of the Central Asian Orogenic Belt, *J. Geol. Soc.*, *164*(1), 31–47, doi:10.1144/0016-76492006-022.
Wright, T., B. Parsons, and E. J. Fielding (2001), Measurement of interseismic strain accumulation across the North Anatolian fault by satellite radar interferometry, *Geophys. Res. Lett.*, *28*(10), 2117–2120, doi:10.1029/2000GL012850.
Wright, T. J., B. Parsons, P. C. England, and E. J. Fielding (2004), InSAR observations of low slip rates on the major faults of western Tibet, *Science*, *305*(5681), 236–239, doi:10.1126/science.1096388.
Yudakhin, F. N. (1986), Pre-Mesozoic Rocks: Density, in *Lithosphere of the Tien Shan*, edited by I. E. Gubin, 156 pp., Nauka, Moscow.
Zubovich, A. V. et al. (2010), GPS velocity field for the Tien Shan and surrounding regions, *Tectonics*, *29*, TC6014, doi:10.1029/2010TC002772.

B. Bookhagen, Department of Geography, University of California, 1832 Ellison Hall, Santa Barbara, CA 93106, USA.
D. W. Burbank and J. K. Goode, Department of Earth Science, University of California, 1006 Webb Hall, Santa Barbara, CA 93106, USA. (jgoode@eri.ucsb.edu)